High Power Laser Science and Engineering, (2025), Vol. 13, e43, 10 pages.
doi:10.1017/hpl.2025.34

HIGH POWER LASER SCIENCE AND ENGINEERING

RESEARCH ARTICLE

Investigating high-energy Hermite–Gaussian and vortex laser generation in alexandrite

Enlin Cai[1,2,3], Shuaiyi Zhang[4], Tao Li[5], Jie Wang[2], and Min Chen[1,2,3]

[1] *Shanghai Institute of Applied Physics, Chinese Academy of Sciences, Shanghai, China*

[2] *Shanghai Advanced Research Institute, Chinese Academy of Sciences, Shanghai, China*

[3] *University of Chinese Academy of Sciences, Beijing, China*

[4] *Shandong Advanced Optoelectronic Materials and Technologies Engineering Laboratory, School of Mathematics and Physics, Qingdao University of Science & Technology, Qingdao, China*

[5] *School of Information Science and Engineering, and Shandong Provincial Key Laboratory of Laser Technology and Application, Shandong University, Qingdao, China*

(Received 17 February 2025; revised 13 March 2025; accepted 25 March 2025)

Abstract

This paper presents an investigation of the secondary saturation characteristics of a $HfTe_2$ saturable absorber. Pulse energies of 5.85 and 7.4 mJ were demonstrated with a high-order Hermite–Gaussian (HG) laser and a vortex laser, respectively, using alexandrite as the gain medium. To the best of our knowledge, these are the highest pulse energies directly generated with HG and vortex lasers. To broaden the applications of high-energy pulsed HG and vortex lasers, wavelength tuning in the region of 40 nm was achieved using an etalon.

Keywords: high-energy pulse laser; reverse saturable absorption; structured light field; wavelength tuning

1. Introduction

The intensity and phase distributions of high-order Hermite–Gaussian (HG) beams allow them to transmit more information than those of Gaussian beams, and so they have important applications in fields such as laser capacity communications, optical measurement and optical manipulation[1–4]. In addition, high-order HG beams can be transformed into vortex beams carrying an orbital angular momentum (OAM) of $l\hbar$ (with l being the quantum number and $\hbar$ the reduced Planck constant), further broadening their applicability[5–7]. Structured light fields generated by high-energy high-order HG lasers have a great deal of benefits over unstructured light[8–12]. However, high-order HG lasers have thus far primarily been confined to a low-energy range, owing to the limitations imposed by the damage threshold and the efficiency of existing generation techniques. The extra-cavity generation method for structured light field relies on phase modulation, which has proven to be inadequate for producing a stably propagating high-order HG mode laser. This limitation stems from the fact that such extra-cavity implementations merely execute the user-programmed photonic design without demonstrating intrinsic evolutionary capabilities, thereby failing to achieve the dynamic characteristics necessary of an active system. In addition, the converters employed for this method are not sufficiently robust to withstand the impact of a high-energy laser[13,14]. The intra-cavity method primarily achieves vortex laser generation by adjusting the gain of different modes. However, etching spot-defects on the input mirror has not yet succeeded in producing high-order HG lasers, and this technique typically reduces the utilization efficiency of the pump laser[15–19]. Consequently, it is essential to develop a method that can generate high-order HG lasers with stable propagation and high efficiency, while remaining unaffected by damage threshold limitations. In 2024, Tao *et al.*[20] theoretically demonstrated that high-order HG lasers with low loss characteristics can be generated using a segmented mirror. This indicates that etching stripes of various shapes and dimensions onto the output mirror is a feasible method for the generation of high-order HG lasers, without affecting the incidence efficiency of the pump laser.

Suitable gain media and laser regulation methods are indispensable for the production of high-energy

Correspondence to: M. Chen, Shanghai Advanced Research Institute, Chinese Academy of Sciences, Shanghai 201800, China. Email: chenm@sari.ac.cn; S. Zhang, Shandong Advanced Optoelectronic Materials and Technologies Engineering Laboratory, School of Mathematics and Physics, Qingdao University of Science & Technology, Qingdao 266061, China. Email: shuaiyi163@163.com

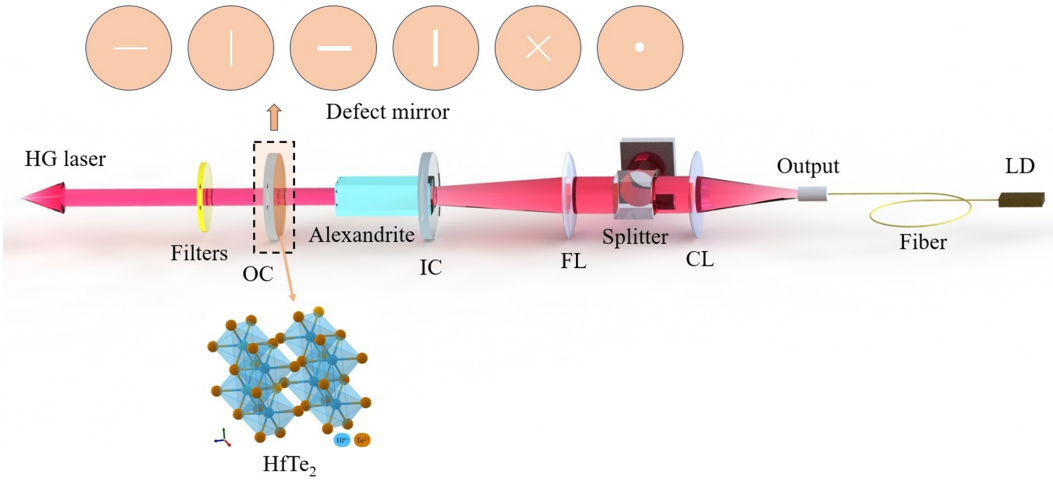

Figure 1. Schematic diagram of the generation of a high-energy Hermite–Gaussian laser. LD, laser diode; CL, collimating lens; FL, focusing lens; IC, input coupler; OC, output coupler. Inset: defect stripes at the OC and crystal structure of $HfTe_2$.

pulsed lasers. Within the visible spectrum, alexandrite (Cr^{3+}:$BeAl_2O_4$) is regarded as an exceptional medium for creating a high-energy pulsed laser, as a result of its superior thermal conductivity, high saturation energy density, robust damage threshold and long fluorescence lifetime[21–23]. Furthermore, the effective gain cross-section of alexandrite crystals increases with temperature, facilitating efficient high-power pumping. In 2023, Liang *et al.*[24] successfully obtained a high-energy pulse of 2.6 mJ in alexandrite using acousto-optic *Q*-switching, highlighting the potential of this method for high-energy operation. Passive *Q*-switching (PQS) is an effective technique for producing pulsed lasers, offering the advantages of a compact design that does not need an external driver. However, PQS typically struggles to achieve high pulse energies, owing to the low saturable fluence of saturable absorbers (SAs), particularly when using two-dimensional (2D) SAs[25–27]. It is worth noting that light absorption by excited state energy levels causes the transmittance of specific 2D materials to decrease only under excitation by extremely high-intensity light. This phenomenon is known as reverse saturable absorption[28]. Nevertheless, excited state absorption in 2D materials can also reach saturation, in a condition referred to as secondary saturation. Compared with ground state absorption saturation, a significantly higher excitation intensity is required to achieve this condition in an excited state. Therefore, SAs with secondary saturation characteristics typically exhibit a higher saturable fluence, which may alleviate the challenges of generating high-energy pulsed lasers through the PQS method.

In this paper, the secondary saturation characteristics of a high-quality, custom-made $HfTe_2$ SA, which has a high damage threshold, were demonstrated using the open aperture Z-scan method. By employing a defect output mirror and a reverse saturable absorber (RSA) $HfTe_2$, high-order HG pulsed lasers of various orders with a maximal single pulse energy of 5.85 mJ and a vortex laser with a single pulse energy of 7.4 mJ were obtained in alexandrite. The repetition rates of these lasers were 262 and 196 Hz, respectively. To expand the applications of high-energy structured lasers, wavelength tuning within the range of 747–787 nm was successfully accomplished using an etalon.

2. Experimental setup

A schematic diagram of the high-energy HG alexandrite laser is shown in Figure 1. The pump laser is a laser diode (LD) with an emission wavelength of 638 nm, offering higher quantum efficiency compared to other pump wavelengths. Owing to the polarization-dependent absorption properties of alexandrite, the pump laser is directed through a polarization beam splitter to enhance the pumping efficiency. The coupling system consists of a collimating lens (CL) and a focusing lens (FL), with focal lengths of 100 and 50 mm, respectively. The pump laser is focused through a coupling system, generating a circular spot with a diameter of 200 μm within the crystal. Both the input coupling and the output coupling are implemented using plane mirrors to maintain the beam quality of the output laser. The alexandrite crystal, with a Cr^{3+} doping concentration of 0.2%, was precision-cut to dimensions of 3 mm × 3 mm × 8 mm and finely polished. The optical path surfaces are coated with a high transmittance for a 755 nm laser. The transmittance of the output coupler (OC) is fixed at 3% and defect stripes of diverse widths and shapes were introduced, as shown in Figure 1, in order to permit the laser to pass through without being reflected, such that only the laser modes that overlap with the no-defect area can be effectively amplified. The output laser is directed through a bandpass filter to obtain high-purity HG modes, free from interference with the pump laser. The $HfTe_2$ absorber was coated onto the OC to achieve *Q*-switching and to minimize resonant cavity loss.

https://doi.org/10.1017/hpl.2025.34 Published online by Cambridge University Press

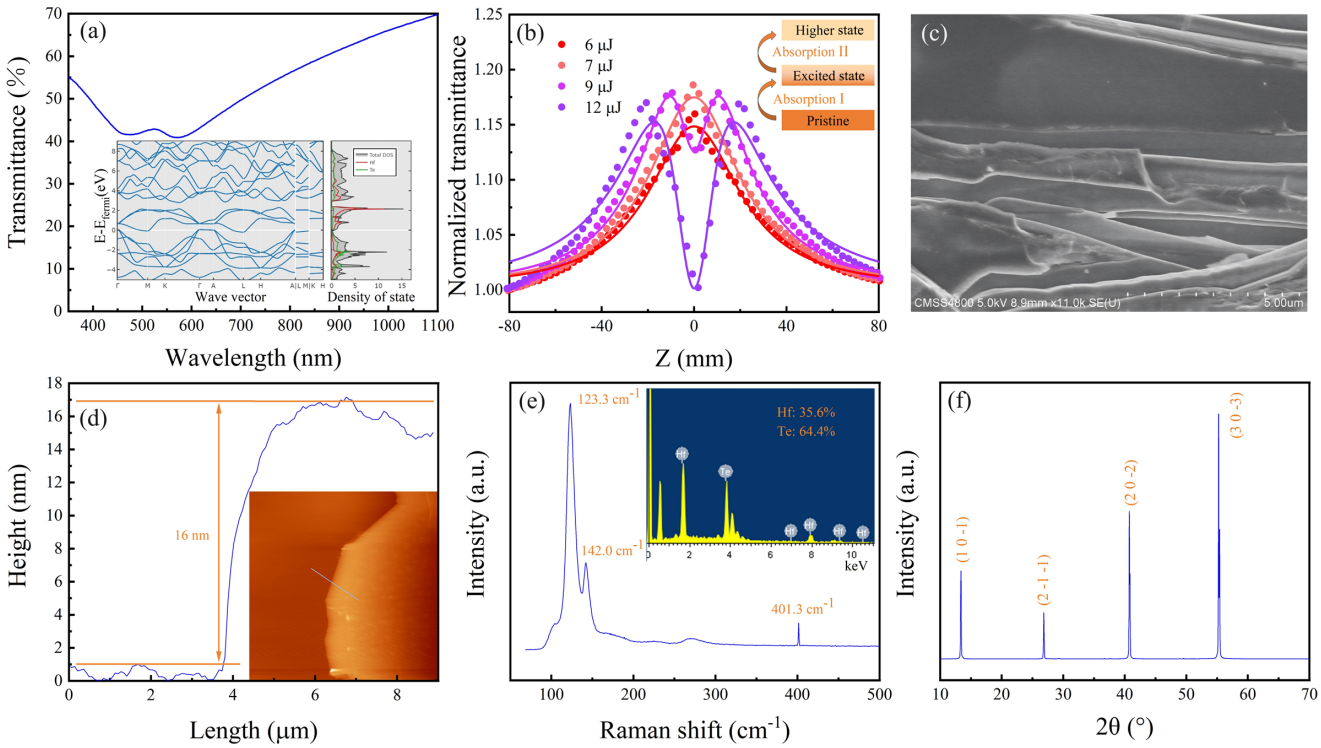

Figure 2. (a) Light transmittance of $HfTe_2$ in the wavelength range of 350–1100 nm. Inset: energy band structure and density of states of $HfTe_2$. (b) Saturation absorption and reverse saturation absorption results of $HfTe_2$ based on an open aperture Z-scan. Inset: the principle of saturation absorption and reverse saturation absorption process. (c) Surface microstructure of $HfTe_2$ by SEM. (d) Thickness of single-layer $HfTe_2$ nanosheets by AFM. Inset: the AFM height image in the area of 30 μm × 30 μm. (e) Raman spectrum of $HfTe_2$. Inset: EDS element analysis. (f) XRD pattern of $HfTe_2$.

The optical transmittance of $HfTe_2$ across the wavelength range of 350–1100 nm is shown in Figure 2(a), demonstrating its strong absorption of visible and near-infrared light. The band energy structure and electron density of $HfTe_2$ are depicted in the inset of Figure 2(a), revealing its zero-bandgap structure. Upon incidence of a laser on $HfTe_2$, electrons in the pristine state are excited to the excited state (Absorption I). Increasing the incident laser power causes a greater number of electrons to populate the excited state. Due to Pauli blocking, which limits the electron occupation in this state, Absorption I reaches saturation and the material ceases to absorb additional laser energy. However, under excitation from a stronger laser, electrons in the excited state will transition to a higher energy state (Absorption II). This process is known as reverse saturation absorption. With further increases in incident laser intensity, the higher energy state may also become saturated as a result of electron accumulation and the wide energy bandgap, which impedes the relaxation process from the higher state back to the excited state, thereby ceasing further laser absorption. The characteristics of saturable absorption and reverse saturation absorption under high-energy excitation are demonstrated in Figure 2(b) via the open aperture Z-scan method with an 800 nm femtosecond laser, confirming that $HfTe_2$ exhibits reverse saturation absorption properties. Figure 2(c) presents the surface microstructure of $HfTe_2$, as examined by scanning electron microscopy (SEM), clearly showing its layered structure. The height of a single-layer $HfTe_2$ nanosheet obtained by mechanical exfoliation, and measured by atomic force microscopy (AFM), was 16 nm, as shown in Figure 2(d). The purity of $HfTe_2$ was analyzed by Raman spectroscopy and an energy dispersive spectrometer (EDS), as shown in Figure 2(e) and the inset. The peaks of the Raman spectrum are located at 123.3, 142.0 and 401.3 cm^{-1}, corresponding to the characteristic Raman peaks of $HfTe_2$. The EDS results indicate that the composition consists of 35.6% Hf and 64.4% Te, with no other elements detected. The growth direction of $HfTe_2$ was characterized by X-ray diffraction (XRD), with diffraction peaks observed at 2θ angles of 13.4°, 26.8°, 40.8° and 55.4°, corresponding to the (1, 0, –1), (2, –1, –1), (2, 0, –2) and (3, 0, –3) growth directions, respectively, as shown in Figure 2(f).

3. Characteristics of the high-energy structured light field

The far-field intensity patterns of HG lasers of different orders and their corresponding defects on the OC are shown, respectively, in Figures 3(a) and 3(b). The defects, introduced by mechanical etching, allow the laser to pass through without undergoing oscillation. The etched defects

https://doi.org/10.1017/hpl.2025.34 Published online by Cambridge University Press

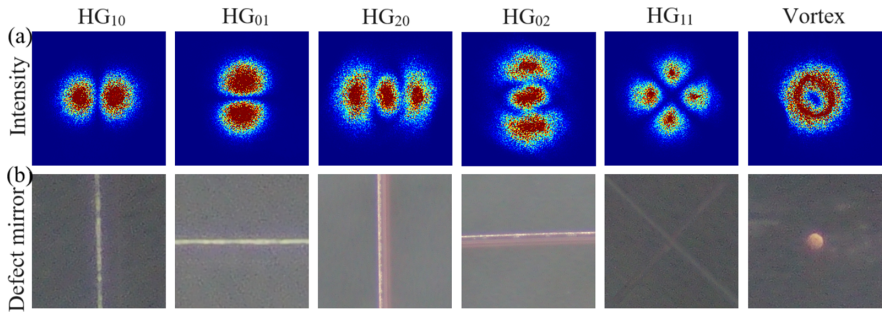

Figure 3. (a) The far-field intensity distribution of Hermite–Gaussian lasers of different orders and the vortex laser. (b) The corresponding defect areas on the output coupling mirror.

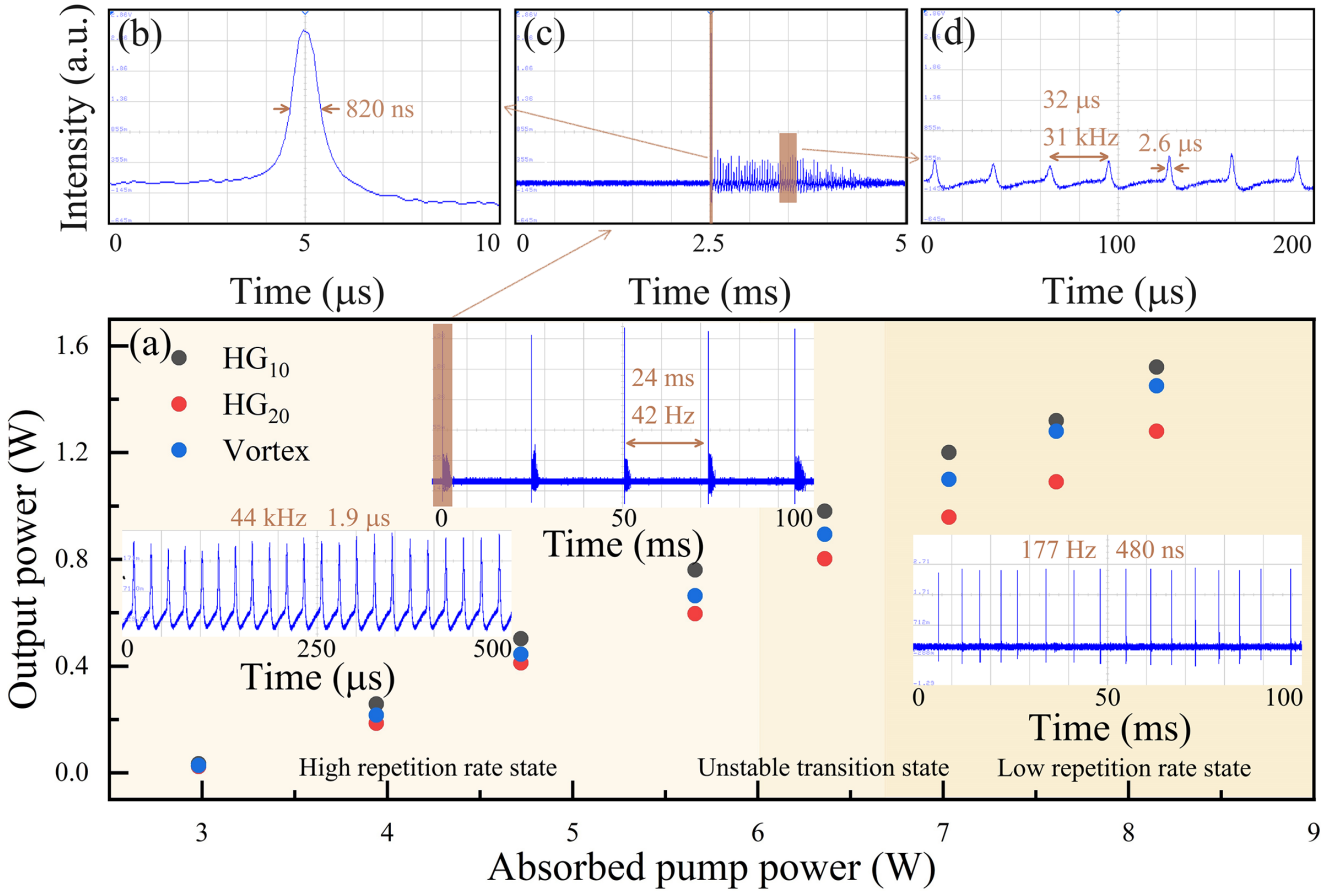

Figure 4. (a) Output characteristics of high-energy HG_{10}, HG_{20} laser and vortex laser. Transition state pulse of the HG_{10} laser at (b) 10 μs; (c) 5 ms; (d) 200 μs scales.

are placed on a red-light source and observed under a microscope. The red light can pass through the defects, appearing as bright areas, while the no-defect regions remain dark due to reflection from the film, as illustrated in Figure 3(b). The intensity distribution of the HG laser is recorded by a charge-coupled device (CCD) at a distance of 5 m in the far-field, with the corresponding laser divergence angle being less than 5 mrad. With etched straight lines with a width of 20 μm in the vertical and horizontal directions, the laser is capable of generating HG_{10} and HG_{01} modes, respectively. As the defect width is increased to 60 μm, HG_{20} and HG_{02} modes can be excited. Through the orthogonal cross-etching of two defect stripes, the laser is optimized to produce the HG_{11} mode. In addition, by etching a circular hole in the OC, the laser can produce a ring-shaped vortex laser. However, due to spot size limitations, wider defects inhibit efficient laser oscillation, preventing the generation of higher order HG modes.

The output pulse characteristics of the HG and vortex lasers at different modes are shown in Figure 4. Since the

https://doi.org/10.1017/hpl.2025.34 Published online by Cambridge University Press

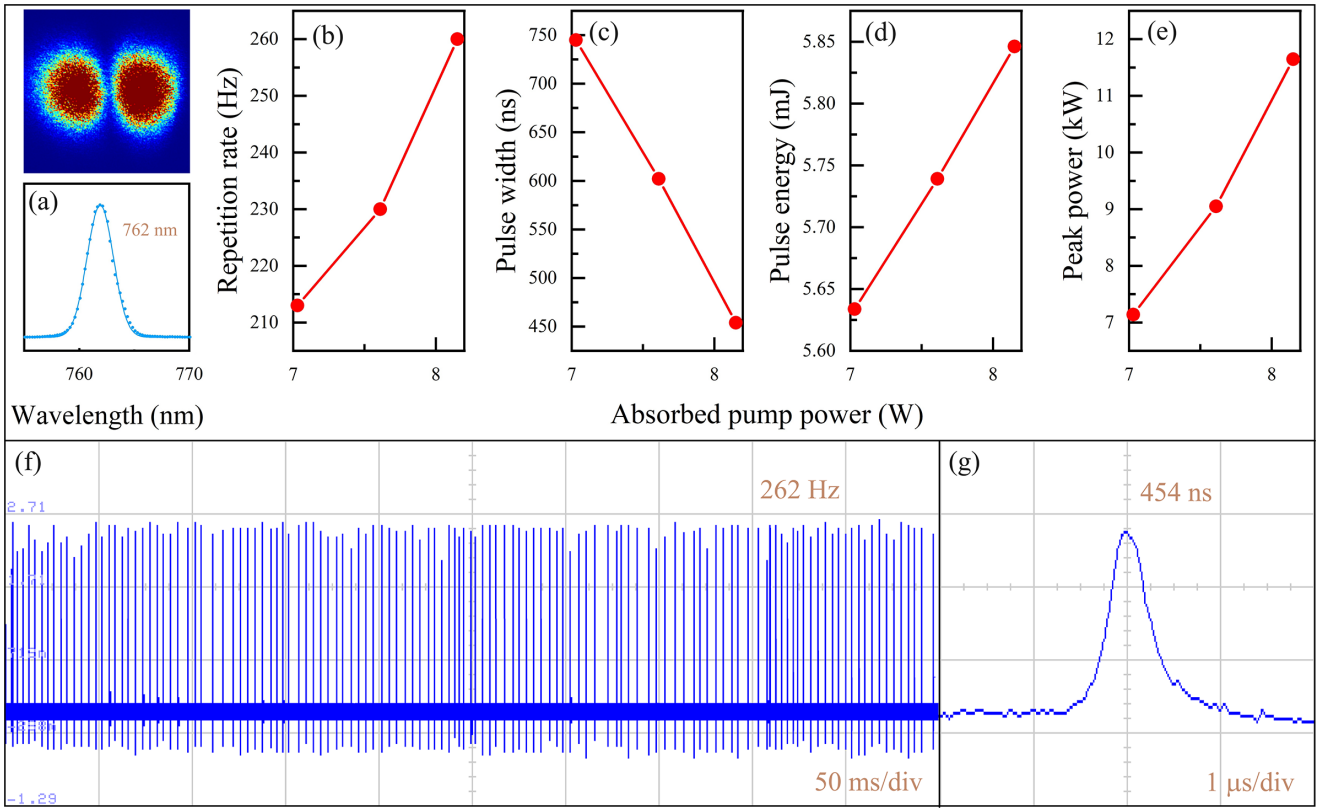

Figure 5. (a) Spectrum. (b) Repetition rate. (c) Pulse width. (d) Pulse energy. (e) Peak power of the HG_{10} mode versus absorbed pump power at the low-repetition-rate state. (f) Typical *Q*-switched pulse train and (g) temporal pulse shape of the HG_{10} mode at maximum average output power.

HG_{10} and HG_{01}, HG_{20} and HG_{02}, as well as HG_{11} and vortex modes exhibit similar output power, repetition rate and pulse width, this work only presents the laser characteristics of the HG_{10}, HG_{20} and vortex modes. The vortex laser operates in two stable states characterized by a high-repetition-rate state (>10 kHz) and a low-repetition-rate state (<300 Hz), as well as an unstable transition state, as described in Figure 4(a). The threshold absorbed pump power is 3.0 W, and it operates in the high-repetition-rate state until the absorbed pump power exceeds 6.0 W. As the absorbed pump power increases, the repetition rate increases and the pulse width decreases gradually within the high-repetition-rate state. For the HG_{10} mode, the maximum repetition rate reaches 44 kHz with a pulse width of 1.9 µs at 6.0 W of absorbed pump power, as shown in Figure 4(a). As the absorbed pump power exceeds 6.0 W, Absorption I reaches a supersaturated state, resulting in high-repetition-rate pulses, and the laser enters an unstable transition state. During the transition state, while emitting high-energy, high-repetition-rate pulses, Absorption II also consumes the excited state electrons, causing Absorption I to no longer remain saturated. Consequently, the high-repetition-rate pulses reappear, as shown in Figure 4(a). As the pump power increases, the excited state is populated more rapidly, effectively sustaining a continuous saturation state, which results in the disappearance of the high-repetition-rate pulses. The low-repetition-rate pulse interval in the transition state is 24 ms, corresponding to a repetition rate of 42 Hz, with a pulse width of 820 ns, as depicted in Figure 4(b). The high-repetition-rate pulses in this state have a repetition rate of 31 kHz and a pulse width of 2.6 µs. Notably, the repetition rate of the high-repetition-rate pulses in the unstable transition state is lower than that in the high-repetition-rate state. This reduction is due to Absorption II decreasing the transmittance of the SA during the modulation of the high-repetition-rate pulse. The repetition rate of the low-repetition-rate pulse in the unstable transition state is also lower than that in the low-repetition-rate state, because the high-repetition-rate pulse consumes electrons in the excited state. When the absorbed pump power exceeds 6.2 W, Absorption I remains in a supersaturated state, and pulse generation depends exclusively on modulation by Absorption II, leading to low-repetition-rate pulses. Figure 4(a) illustrates a typical low-repetition-rate pulse with a repetition rate of 177 Hz and a pulse width of 480 ns, demonstrating superior stability in both pulse repetition and intensity compared to the high-repetition-rate pulses.

The low-repetition-rate state pulse laser characteristics of the HG_{10} mode are presented in Figure 5. Figure 5(a) shows the spectrum of the *Q*-switched pulse laser, with a central wavelength at 762 nm and a full width at half maximum (FWHM) of 3 nm at the maximum absorbed

https://doi.org/10.1017/hpl.2025.34 Published online by Cambridge University Press

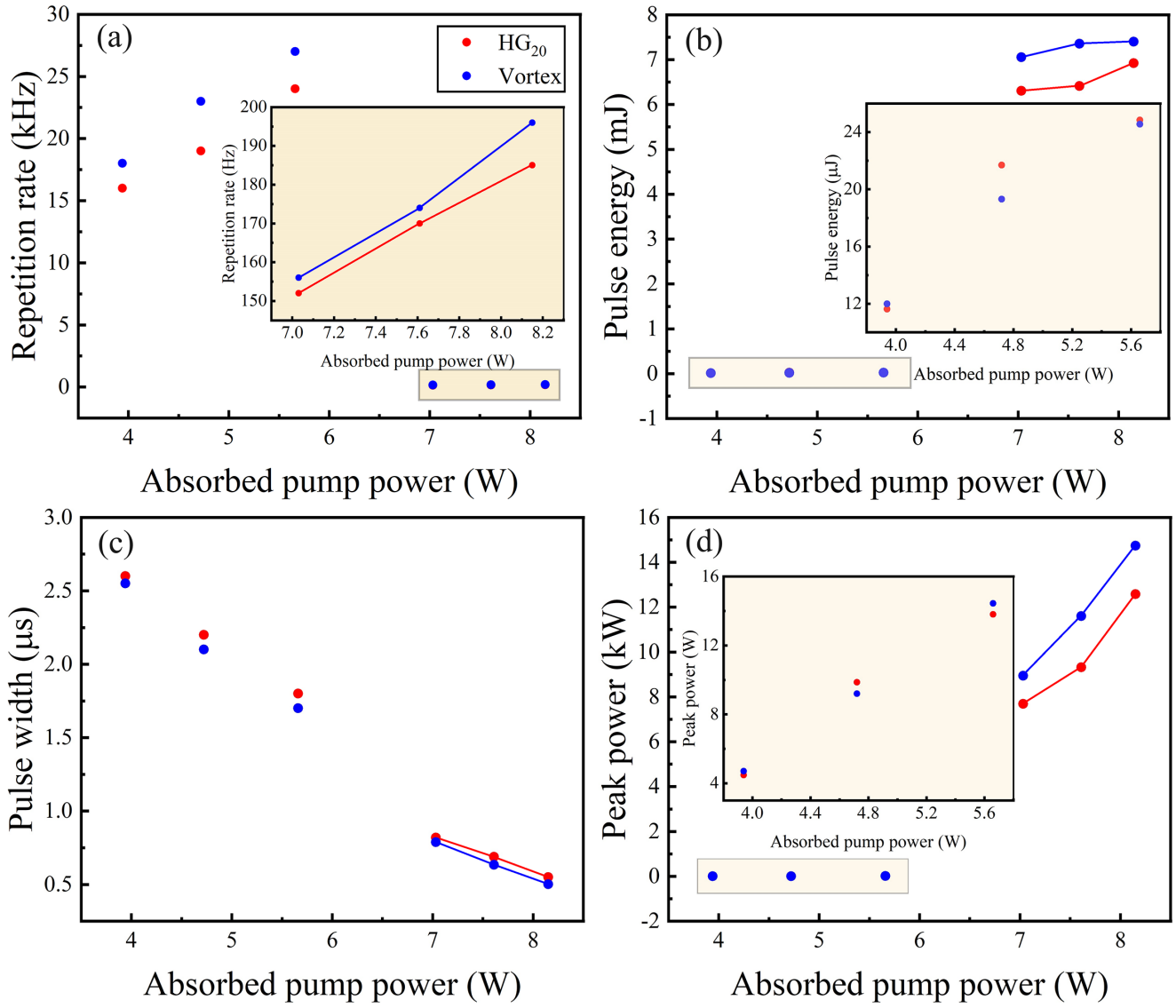

Figure 6. (a) Repetition rate. (b) Pulse energy. (c) Pulse width. (d) Peak power of HG_{20} and vortex mode laser versus absorbed pump power.

pump power of 8.15 W. As the absorbed pump power increases, the repetition rate increases while the pulse width decreases gradually. When the absorbed pump power was 8.15 W, the maximum repetition rate and the narrowest pulse width were 262 Hz and 454 ns, respectively, as depicted in Figures 5(f) and 5(g). The single pulse energy and peak power also increased gradually with the absorbed pump power, and the maximum pulse energy reached 5.85 mJ, corresponding to a peak power of 11.6 kW. The single pulse energy density and peak power density in the gain medium were 12.2 J/mm^2 and 24.3 MW/mm^2, respectively. Notably, the performance of the $HfTe_2$ SA is not compromised by the impact of such a high-energy pulse. Typical pulse trains and temporal pulse profile are displayed in Figures 5(f) and 5(g) in the time ranges of 0.5 s and 4 μs. Figure 5(f) demonstrates that the pulse train has good repeatability and relatively consistent peak intensity. The remarkable pulse stability originates from two key aspects. Firstly, the high saturation intensity of the excited state absorption process increases the cavity loss, which promotes the generation of stable pulses and provides substantial fault tolerance. Secondly, the intrinsic stability of the material structure combined with its well-defined energy level structure ensures consistent laser performance.

The laser characteristics of the HG_{20} and vortex modes are shown in Figure 6. Figure 6(a) illustrates the variation of the repetition rate with absorbed pump power in both the high- and low-repetition-rate states. In the high-repetition-rate state, the highest repetition rates were 24 kHz for the HG_{20} mode and 28 kHz for the vortex mode, respectively, while these rates dropped sharply to 185 and 196 Hz in the low-repetition-rate mode. The corresponding pulse energy also increased from 24.8 μJ to 6.92 mJ for the HG_{20} mode and from 24.6 μJ to 7.40 mJ for the vortex mode, respectively,

https://doi.org/10.1017/hpl.2025.34 Published online by Cambridge University Press

Table 1. Comparative characteristics of *Q*-switched high-order HG and vortex mode lasers.

Mode	Wavelength	Gain medium (SA)	Output power	Pulse energy	Reference
HG	1064 nm	Nd:YAG (Cr:YAG)	1.32 W	22 μJ	[29]
HG	1079 nm	Nd:LYSO (Cr:YAG)	1.96 W	63 μJ	[30]
HG	1064 nm	Nd:YAG (Cr:YAG)	780 mW	3 μJ	[31]
HG	2018.3 nm	Tm:LuYAG (active)	870 mW	1.51 mJ	[32]
Vortex	607 nm	Pr:YLF (Co:ASL)	139 mW	0.89 μJ	[33]
Vortex	639 nm	Pr:YLF (Co:ASL)	1.35 W	2.5 μJ	[34]
Vortex	1064 nm	Nd:YAG (Ag:LNOI)	130 mW	23.4 nJ	[35]
Vortex	1064 nm	Nd:YAG (Cr:YAG)	760 mW	18 μJ	[36]
Vortex	1063 nm	Nd:$GdVO_4$ (active)	9.38 W	469 μJ	[37]
Vortex	1647.7 nm	Er:LuYAG (active)	940 mW	660 μJ	[38]
Vortex	1937.9 nm	Tm:YAP (self)	83 mW	1.1 μJ	[39]
Vortex	2 μm	Tm:$YALO_3$ (self)	4.8 W	38.8 μJ	[40]
HG	762 nm	Alexandrite ($HfTe_2$)	1.52 W	5.85 mJ	This work
Vortex	762 nm	Alexandrite ($HfTe_2$)	1.48 W	7.40 mJ	This work

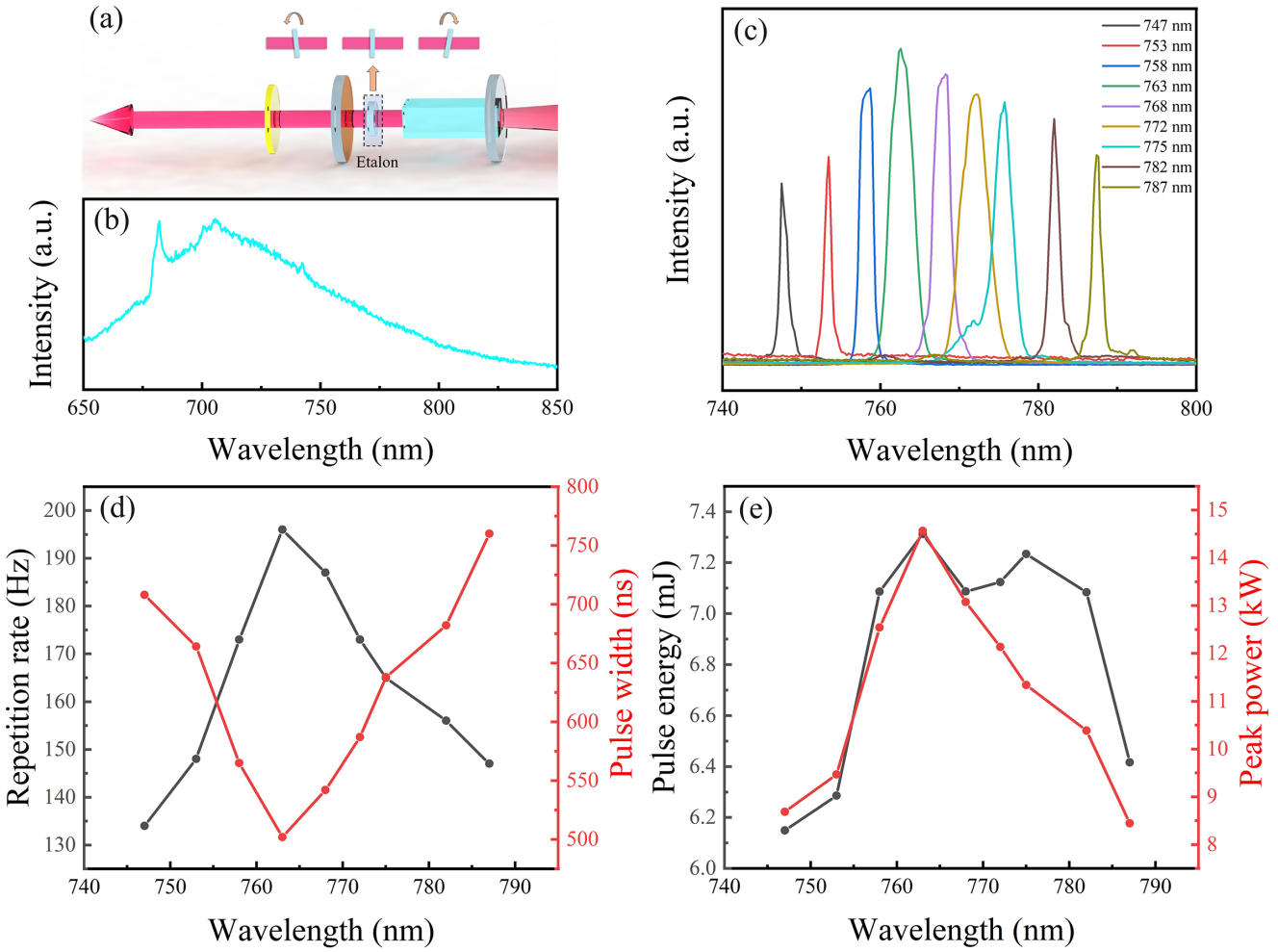

Figure 7. (a) Schematic diagram of wavelength-tunable *Q*-switched vortex laser based on an etalon. (b) Fluorescence spectrum of alexandrite excited by a 638 nm pump laser. (c) Laser spectra and relative intensities at different wavelengths within the alexandrite wavelength tuning range. (d) Repetition rate and pulse width. (e) Pulse energy and peak power of passively *Q*-switched vortex laser versus wavelength.

as depicted in Figure 6(b), proving that Absorption II has a higher saturation flux and can accommodate more electrons due to its wider energy band. As shown in Figure 6(c), the pulse width of both the HG_{20} and vortex modes decreased slowly with increasing absorbed pump power, even across different states. The narrowest pulse widths reached 550 ns for the HG_{20} mode and 502 ns for the vortex mode at the maximum absorbed pump power of 8.15 W.

https://doi.org/10.1017/hpl.2025.34 Published online by Cambridge University Press

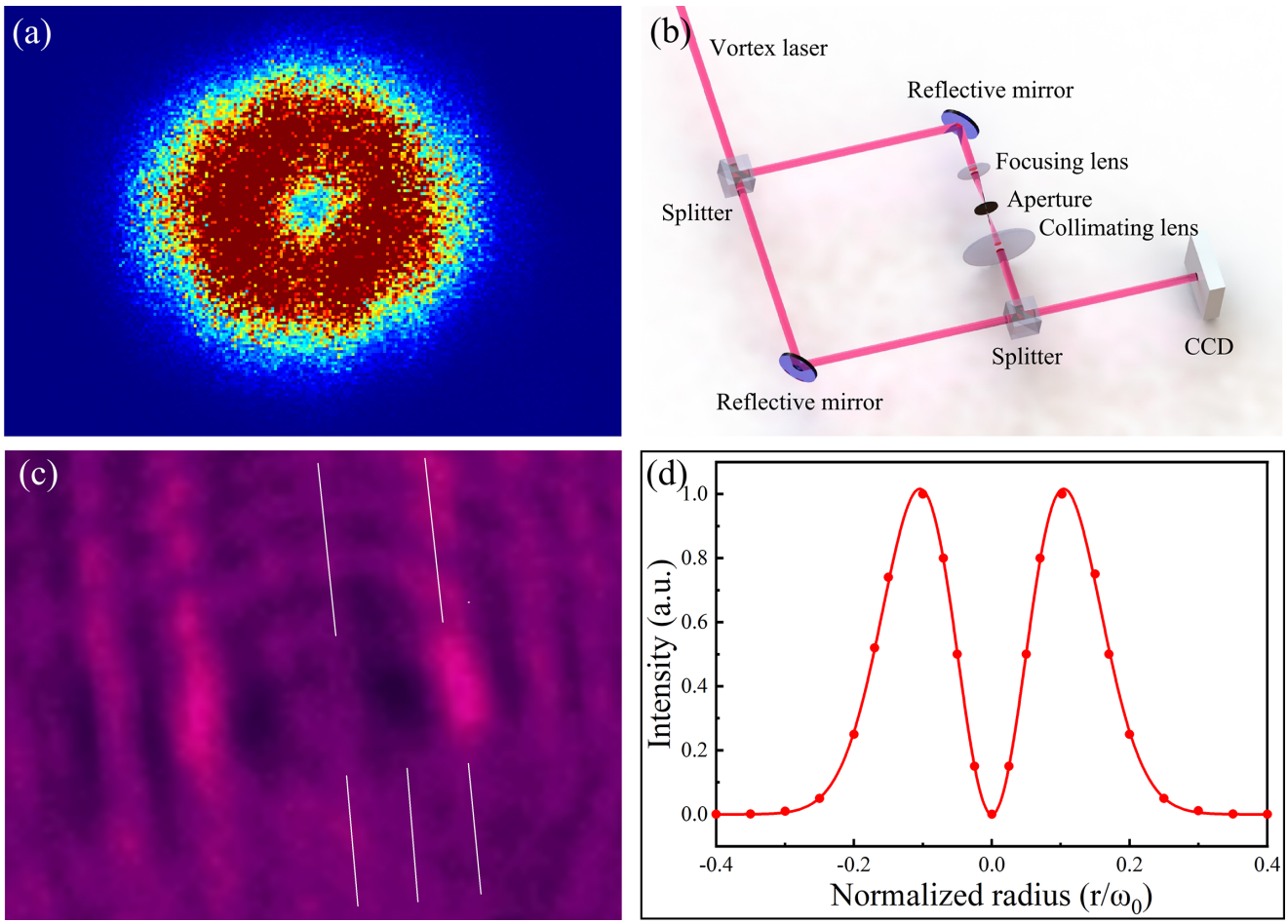

Figure 8. (a) Typical intensity profile of the high-energy vortex pulse laser. (b) Mach–Zehnder interferometer for characterizing the topological charge of the optical vortex. (c) Beam profile interference patterns for the vortex laser. (d) Experimentally measured transverse intensity profile and its theoretical fit.

Table 1 summarizes the characteristics of typical *Q*-switched high-order HG and vortex lasers. It can be seen that our experimental approach yields the highest pulse energy compared with other gain media and modulation methods. Nonetheless, it is particularly appropriate for the generation of high-energy HG pulses at short wavelengths.

4. Wavelength tuning characteristics

Since a 750–785 nm laser corresponds to the absorption peak of Rb atoms, and has a larger penetration depth in biological tissues, this wavelength range has a wide range of applications including laser medical treatment, cold atoms and laser pumping[41–50]. In particular, the 780 nm vortex laser has indispensable applications, such as cold atomic clocks, hot atomic steam and cold atom storage, but it can only be produced through extra-cavity modulation[42,43]. To expand the utility of high-energy HG and vortex lasers, an etalon was employed for wavelength tuning based on an alexandrite crystal, which has a wide emission spectrum, as shown in Figure 7(b).

The schematic diagram of a wavelength-tunable *Q*-switched vortex alexandrite laser is depicted in Figure 7(a). By utilizing a 0.2 mm thick etalon rotated within a tilt angle of 10°, continuous wavelength tuning can be achieved across the range of 747–787 nm. The relative intensity and FWHM at different wavelengths are shown in Figure 7(c). The FWHM of the spectrum is 3 nm at a central wavelength of 763 nm, while it narrows to 1 nm at the wavelengths of 747 and 787 nm due to the optical filtering effect of the etalon. In addition, Figure 7(d) presents the corresponding repetition rates and pulse widths at various wavelengths at an absorbed pump power of 8.15 W. As the intra-cavity power diminishes, the repetition rate decreases and the pulse width increases. The repetition rate and pulse width of the 747 nm pulsed vortex laser were 134 Hz and 708 ns, respectively, while those of the 787 nm pulsed vortex laser were 147 Hz and 760 ns, respectively. The pulse energy and peak power show a dependence on the gain during the process of wavelength tuning. As shown in Figure 7(e), the pulse energy and peak power of the 747 nm pulsed vortex laser were 6.15 mJ and 8.69 kW, respectively. Meanwhile, for the 787 nm pulsed vortex laser, the pulse energy and peak power were 6.42 mJ

https://doi.org/10.1017/hpl.2025.34 Published online by Cambridge University Press

and 8.44 kW, respectively. The wavelength tuning range was restricted by the coating constraints of the resonant cavity mirrors.

As illustrated in Figure 8(a), the typical intensity profile of the high-energy vortex pulse laser displays a distinctive annular light intensity pattern. To characterize the phase distribution and OAM carried by the output vortex laser, a custom-built Mach–Zehnder interferometer device was employed. The output intensity distribution was collected and analyzed using a CCD, as depicted in Figure 8(b). Figure 8(e) shows the interference pattern of the vortex laser. The typical fork-shape stripe indicates that the vortex laser has a negative helical direction with a topological charge of –1. To verify the purity of the vortex mode laser, the transverse intensity profile of the vortex mode along the x-axis was measured, as shown in Figure 8(d). The experimentally measured intensity curve is theoretically fitted by using a first-order vortex function

$$\frac{I}{I_0} = A\frac{2r^2}{\omega_0^2}\exp\left(-\frac{r^2}{\omega_0^2}\right),$$

where $\frac{I}{I_0}$ is the normalized intensity, A is a constant and ω_0 is the beam waist. The transverse intensity profile closely matches the theoretical fit based on the first-order vortex function, indicating excellent mode purity.

5. Conclusion

This paper has presented the first successful generation of high-energy pulsed HG and vortex lasers, using the mechanical etching defect method in conjunction with RSA $HfTe_2$. At an absorbed pump power of 8.15 W, the single pulse energy of the HG_{10} laser reached 5.85 mJ with an average output power of 1.52 W. The single pulse energy of the vortex laser was 7.4 mJ, with an average output power of 1.48 W and a low repetition rate of 196 Hz. To the best of our knowledge, this is the highest single pulse energy obtained by the intracavity generation method. In addition, our work analyzes and verifies the advantages of the reverse saturable absorption effect in the generation of high-energy pulses. Using an etalon, vortex pulse lasers with a tunable wavelength range of 747–787 nm were realized, thereby expanding the potential applications of high-energy HG and vortex lasers.

Acknowledgements

The authors thank the staff at the beamline BL06B at Shanghai Synchrotron Radiation Facility (SSRF) for their experimental assistance.

This work was supported by the National Natural Science Foundation of China (Grant Nos. 12204499 and 12174212) and the Joint Key Projects of National Natural Science Foundation of China (Grant No. U2032206).

References

1. S. Restuccia, D. Giovannini, G. Gibson, and M. Padgett, Opt. Express **24**, 27127 (2016).
2. K. Pang, H. Song, Z. Zhao, R. Zhang, H. Song, G. Xie, L. Li, C. Liu, J. Du, A. F. Molisch, M. Tur, and A. E. Willner, Opt. Lett. **43**, 3889 (2018).
3. Y. Turek, H. Kobayashi, T. Akutsu, C. P. Sun, and Y. Shikano, New J. Phys. **17**, 083029 (2015).
4. S. Al-Awfi, S. Bougouffa, and M. Babiker, Opt. Commun. **283**, 1022 (2010).
5. H. Liu, L. Yan, H. Chen, X. Liu, H. Liu, S. H. Chew, A. Gliserin, Q. Wang, and J. Zhang, Light Sci. Appl. **12**, 207 (2023).
6. G. Liang and Q. Wang, Opt. Express **27**, 10684 (2019).
7. H. C. Liang, Y. J. Huang, Y. C. Lin, T. H. Lu, Y. F. Chen, and K. F. Huang, Opt. Lett. **34**, 3842 (2009).
8. J. Hamazaki, R. Morita, K. Chujo, Y. Kobayashi, S. Tanda, and T. Omatsu, Opt. Express **18**, 2144 (2010).
9. C. Hnatovsky, V. G. Shvedov, W. Krolikowski, and A. V. Rode, Opt. Lett. **35**, 3417 (2010).
10. O. J. Allegre, Y. Jin, W. Perrie, J. Ouyang, E. Fearon, S. P. Edwardson, and G. Dearden, Opt. Express **21**, 21198 (2013).
11. D. Liu, Z. Kuang, W. Perrie, P. J. Scully, A. Baum, S. P. Edwardson, E. Fearon, G. Dearden, and K. G. Watkins, Appl. Phys. B **101**, 817 (2010).
12. K. Miyamoto, S. Miyagi, M. Yamada, K. Furuki, N. Aoki, M. Okida, and T. Omatsu, Opt. Express **19**, 12220 (2011).
13. L. L. N. Thi, K. F. Tsai and S. C. Chu, Photonics **11**, 563 (2024).
14. V. Peet, J. Opt. **12**, 095706 (2010).
15. X. Zhu, J. Yang, Y. Chen, H. He, and J. Dong, Opt. Laser Technol. **180**, 111584 (2025).
16. L. Hai, Z. Zhang, S. Liu, L. Li, Z. Zhou, Q. Wang, Y. Gao, C. Gao, Y. Shen, and S. Fu, Laser Photonics Rev. **18**, 2300593 (2024).
17. T. Bell, M. Kgomo, and S. Ngcobo, Opt. Express **28**, 16907 (2020).
18. Q. Yang, Z. Yang, D. Cai, X. Ren, C. Li, Y. Zu, S. Z. U. Din, J. Leng, J. Liu, and J. He, Opt. Express **30**, 23909 (2022).
19. A. Ito, Y. Kozawa, and S. Sato, J. Opt. Soc. Am. A **27**, 2072 (2010).
20. L. Tao, N. Brown, and P. Fulda, J. Opt. **26**, 015603 (2024).
21. E. Cai, S. Zhang, M. Jiang, Q. Liu, F. Lou, H. Lv, and T. Li, Opt. Express **32**, 25463 (2024).
22. J. C. Walling, H. P. Jenssen, R. C. Morris, E. W. O'Dell, and O. G. Peterson, Opt. Lett. **4**, 182 (1979).
23. A. Teppitaksak, A. Minassian, G. M. Thomas, and M. J. Damzen, Opt. Express **22**, 16386 (2014).
24. M. Liang, A. Minassian, and M. J. Damzen, Opt. Express **31**, 42428 (2023).
25. A. I. Chizhikov, A. V. Mukhin, N. A. Egorov, V. V. Gurov, V. Y. Molchanov, N. F. Naumenko, K. V. Vorontsov, K. B. Yushkov, and N. G. Zakharov, Opt. Lett. **47**, 1085 (2022).
26. J. Gong, L. Dong, H. Chu, Z. Pan, H. Pan, Y. Li, S. Zhao, and D. Li, Infrared Phys. Technol. **133**, 104809 (2023).
27. E. Cai, J. Xu, S. Zhang, and Z. Wu, Laser Phys. Lett. **19**, 065802 (2022).
28. Y. Liang, W. Qiao, T. Feng, B. Zhang, Y. Zhao, Y. Song, T. Li, and C. Kränkel, Opt. Express **29**, 23786 (2021).
29. M. Zhang, H. He, and J. Dong, IEEE Photonics J. **9**, 1501214 (2017).

https://doi.org/10.1017/hpl.2025.34 Published online by Cambridge University Press

30. Y. Zhao, Z. Wang, H. Yu, S. Zhuang, H. Zhang, X. Xu, J. Xu, X. Xu, and J. Wang, Appl. Phys. Lett. **101**, 031113 (2012).
31. Y. Chen, C. Chang, C. Lee, C. Sung, J. Tung, K. Su, H. Liang, W. Chen, and G. Zhang, Photonics Res. **5**, 561 (2017).
32. Y. Chen, M. Ding, J. Wang, L. Wang, Q. Liu, Y. Zhao, Y. Liu, D. Shen, Z. Wang, X. Xu, and V. Petrov, Opt. Lett. **45**, 722 (2020).
33. Q. Tian, B. Xu, N. Li, Z. Luo, H. Xu, and Z. Cai, Opt. Lett. **44**, 5586 (2019).
34. N. Li, B. Xu, S. Cui, X. Qiu, Z. Luo, H. Xu, Z. Cai, and L. Chen, IEEE Photonics Technol. Lett. **17**, 1457 (2019).
35. W. Sun, Y. Liu, C. Romero, J. R. V. de Aldana, F. Ren, Y. Jia, X. Sun, and F. Chen, Opt. Express **31**, 36725 (2023).
36. Y. Pan, M. Zhang, and J. Dong, J. Opt. **21**, 085202 (2019).
37. J. Liu, Y. Duan, W. Mao, X. Jin, Z. Li, and H. Zhu, Crystals **13**, 1484 (2023).
38. Q. Liu, Y. Zhao, W. Zhou, and D. Shen, Opt. Mater. **71**, 31 (2017).
39. W. Zhang, L. Tong, Y. Yuan, C. Chen, Y. Cai, and L. Zhao, Infrared Phys. Technol. **123**, 104197 (2022).
40. L. Tong, C. Chen, Y. Cai, and L. Zhao, Materials **17**, 1144 (2024).
41. K. Huang, C. Su, M. Lin, Y. Chiu, and Y. Huang, Opt. Express **24**, 12043 (2016).
42. S. Micalizio, F. Levi, C. E. Calosso, M. Gozzelino, and A. Godone, GPS Solut. **25**, 94 (2021).
43. C. Wang, C. Lee, Y. Kim, and Y.-H. Kim, Opt. Lett. **45**, 1802 (2020).
44. A. J. McCulloch, D. V. Sheludko, M. Junker, and R. E. Scholten, Nat. Commun. **4**, 1692 (2013).
45. M. Kim, R. Notermans, C. Overstreet, J. Curti, P. Asenbaum, and M. A. Kasevich, Opt. Lett. **45**, 6555 (2020).
46. M. Hübner, M. Wilkens, B. Eppich, A. Maaßdorf, D. Martin, A. Ginolas, P. S. Basler, and P. Crump, Opt. Express **29**, 9749 (2021).
47. C. Ke, C. Chen, M. Yang, H. Chen, Y. Ke, and L. Li, Biomed. J. **47**, 100675 (2024).
48. M. Chi, A. Müller, A. K. Hansen, O. B. Jensen, P. M. Petersen, and B. Sump, Opt. Commun. **514**, 128120 (2022).
49. Q. Li, W. Perrie, R. Potter, O. Allegre, Z. Li, Y. Tang, G. Zhu, D. Liu, P. Chalker, and J. Ho, J. Phys. D: Appl. Phys. **53**, 365301 (2020).
50. M. Maiwald, B. Eppich, A. Ginolas, B. Sumpf, G. Erbert, and G. Tränkle, Appl. Spectrosc. **69**, 1144 (2015).

https://doi.org/10.1017/hpl.2025.34 Published online by Cambridge University Press